J. Fluid Mech. (2025), *vol.* 1015, A37, doi:10.1017/jfm.2025.10363

The onset of outer-layer self-similarity in turbulent boundary layers

Jason Appelbaum[1], **Tobias Gibis**[1], **Sergio Pirozzoli**[2] and **Christoph Wenzel**[1]

[1]Institute of Aerodynamics and Gas Dynamics, University of Stuttgart, 70563 Stuttgart, Germany

[2]Dipartimento di Ingegneria Meccanica e Aerospaziale, Sapienza Università di Roma, Via Eudossiana 18, 00184 Rome, Italy

Corresponding authors: Jason Appelbaum, appelbaum@iag.uni-stuttgart.de; Christoph Wenzel, wenzel@iag.uni-stuttgart.de

(Received 3 February 2025; revised 6 May 2025; accepted 10 June 2025)

In this study, changes in the mean flow of a compressible turbulent boundary layer spatially evolving from low to 'moderate' Reynolds numbers are examined. All discussions are based on literature data and a direct numerical simulation (DNS) of a supersonic boundary layer specifically designed to be effectively free of spurious inflow effects in the range $4000 \lessapprox Re_\theta \lessapprox 5000$, which enables discussion of sensitive properties such as the turbulent wake. Most noticeably, the DNS data show the formation of a distinct 'bend' in the friction coefficient distribution reflected in sudden deviation from established low-Reynolds-number correlations. As will be shown, the bend is related to the surprisingly abrupt saturation of the turbulent wake, marking the change from low- to moderate-Reynolds-number behaviour; in previous studies, this trend was potentially obscured by data scatter in experiments and/or insufficient domain length in DNS. Moreover, the influence of the wake saturation on the formation of the early logarithmic overlap layer is assessed, which, if fully developed, leads to the onset of high-Reynolds-number behaviour further downstream.

Key words: turbulent boundary layers, compressible boundary layers, boundary layer structure

1. Introduction

For decades, it has been understood that the Reynolds number (Re) profoundly affects properties of a spatially developing turbulent boundary layer (TBL). Both the mean-velocity profile and the 'structure of turbulence', typically referring to the wall-normal distribution of averaged turbulent stresses, are affected fundamentally by the change in Re regime. For instance, this change manifests itself in a distinctly modified streamwise progression of the friction coefficient $c_f = 2\tau_w/(\rho_\infty u_\infty^2)$ at roughly $4000 \lessapprox Re_\theta \lessapprox 5000$, where τ_w is the averaged wall shear stress, ρ_∞ and u_∞ are the mass density and streamwise velocity of the free-stream flow and $Re_\theta = \theta u_\infty \rho/\mu$ is the Reynolds number formulated with the momentum thickness θ and dynamic viscosity μ. The progression of $c_f(Re_\theta)$ is usually approximated by a corresponding low-Re or high-Re correlation, for example that of Smits, Matheson & Joubert (1983) or the 'Coles–Fernholz 2' correlation of Nagib, Chauhan & Monkewitz (2007). In approximately the same Re range as the change in c_f, the wake parameter (to be defined later) becomes roughly constant. However, such trends are largely based on fits determined from a multitude of numerical and experimental data, potentially hiding finer details due to data scatter. The wake parameter Π in particular (but also c_f) shows a surprisingly strong data scatter as seen in Fernholz & Finley (1980), Panton (2005), Chauhan, Monkewitz & Nagib (2009) and Sanmiguel Vila *et al.* (2017). Historically, such has allowed a consensus as to large-scale trends over a wide Re range, however, clear and detailed discussion about its particular characteristic in the range $4000 \lessapprox Re_\theta \lessapprox 5000$ has not been possible. The mentioned Reynolds-number range represents an effective 'blind spot' rarely covered by both numerical and experimental studies with particular emphasis on the upstream development of the turbulent wake, limiting an accurate discussion of fine edge-to-wall trends.

From a numerical point of view, the principal challenge in obtaining reliable TBL data in this Reynolds-number region (and beyond) is the strong dependence of the boundary-layer properties on the turbulent inflow boundary condition, which has been addressed in Schlatter & Örlü (2012), Sillero, Jiménez & Moser (2013), Sanmiguel Vila *et al.* (2017) and Ceci *et al.* (2022). Whereas the near-wall flow (and thus c_f) generally develops rather quickly to a state with approximately 1−2 % uncertainty, the slow characteristic period of the outer layer can easily take several hundred inflow boundary-layer thicknesses δ_0 to reach a consistent, inflow-independent state, quickly escalating the computational cost of wake-converged direct numerical simulation (DNS) as covered in e.g. Sillero *et al.* (2013) and Ceci *et al.* (2022). If, for instance, a DNS is aimed at covering a targeted Re in the range $4000 \lessapprox Re_\theta \lessapprox 5000$ with a well-developed wake (with respect to metrics like shape factor, etc.), a numerical domain would already have to start at $Re_\theta \approx 780$ if an inflow relaxation length of $200\delta_0$ is to be guaranteed upstream of e.g. $Re_\theta \approx 3000$, allowing some buffer for physical development. Here, $200\delta_0$ can be seen as a rough consensus of recent studies, based on the authors' own assessments, through evaluation of Schlatter & Örlü (2010), Sillero *et al.* (2013) and Eitel-Amor, Örlü & Schlatter (2014) among others. This finding applies particularly to studies using a recycling strategy, which often show a pronounced initial drop in Π immediately downstream of the inlet before slowly converging towards an expected value from below, see Sillero *et al.* (2013) and Ceci *et al.* (2022). Most likely, this drop can be attributed to the fact that traditional recycling approaches only rescale the turbulent flow field in the wall-normal direction but not in the spanwise direction. Consequently, highly reliable DNS of TBLs require careful application of inflow boundary conditions in combination with simulation domains of very large spatial extent that enable the physically representative, inflow-independent evolution of the boundary layer as explored in Wenzel (2019). Mainly due to the sheer computational demand needed to establish an inflow length of $>200\delta_0$ for DNS data reaching $Re_\theta \gtrapprox 4000$, Ceci *et al.* (2022), however, concluded that 'very few studies have used such long domains, which raises questions about the reliability of reference data'.

In a physical experiment, the challenges are not dissimilar to those of numerical simulation in the low-Re regime. For example, the effects of the leading edge of the flat plate or the choice of transition method (natural transition, trip wire, etc.) can influence the boundary-layer growth at low Re considerably, as discussed in e.g. Smits *et al.* (1983) and Erm & Joubert (1991). In addition, local τ_w is difficult to directly measure in experiment, thus c_f is often estimated indirectly through calibration of the streamwise velocity profile based on an assumed logarithmic-layer profile, for example through the Clauser fitting method. The most reliable experimental data for c_f are those which have been obtained using oil-film interferometry (OFI), a technique capable of directly measuring local τ_w, discussed in depth in Fernholz *et al.* (1996). Further difficulties, especially concerning the discussion of the spatial development of the turbulent wake, arise from its sensitivity to uncertainties in the direct determination of τ_w, as well as the practical feasibility of performing measurements with very high streamwise resolution. Perhaps the best-known OFI experiments are those of Österlund *et al.* (2000) and Nagib *et al.* (2006), whose datasets, however, start at $Re_\theta \gtrapprox 6700$ and $Re_\theta \gtrapprox 12\,200$, respectively, thus being well above the 'blind spot' at $4000 \lessapprox Re_\theta \lessapprox 5000$.

1.1. *Objectives*

The primary objective of the present work is to zoom in to the Re range where low-Re and high-Re correlations meet ($4000 \lessapprox Re_\theta \lessapprox 5000$) with a DNS that is likely devoid of spurious inflow effects. To this end, DNS data of a supersonic compressible boundary layer are considered starting at a low inflow Re and ending notably past $Re_\theta \approx 5000$, enabling trends to become clearly visible. Here, the low inflow Re allows the data to be considered effectively free of inlet artefacts by discarding the first $\sim 300\delta_0$ worth of domain extent, as seen in figure 5. Moreover, the downstream state in excess of $Re_\theta \gtrapprox 5000$ allows confirmation of trends established upstream. The main question addressed is: What physical changes occur in the mean flow of the TBL as it develops from a low to moderate Reynolds number, i.e. (i) how clearly can a TBL be characterised as being either a low or moderate Re TBL, or in other words, how distinctly does this change manifest itself in e.g. the c_f distribution? (ii) How clearly can this behaviour be associated with turbulent wake saturation, i.e. the turbulent wake's arrival at a self-similar state? (iii) What is the connection between early moderate-Re behaviour and the early development of the logarithmic layer? By considering all questions in the context of existing literature data, the consistency of the conclusions is strengthened.

Use of a compressible boundary layer in this study is motivated by greater computational efficiency as compared with incompressible solvers which require the solution of a Poisson equation for pressure. In fact, whereas DNS of incompressible boundary layers is still limited to the work of Sillero *et al.* (2013), reaching $Re_\tau \approx 2000$, higher Reynolds numbers have been achieved with DNS of compressible boundary layers (Pirozzoli & Bernardini 2013). Despite obvious differences between low- and high-speed shear layers, evidence is provided that the reported results also extend to the incompressible case.

1.2. *Nomenclature and conventions*

In the present study, the streamwise, wall-normal and spanwise directions are denoted by $[x, y, z]$ respectively. Inlet free-stream values are designated by a subscript '0'. Overlined values ($\bar{f}$) refer to Reynolds-averaged values, where f is an arbitrary quantity. Mean-removed quantities are denoted by a single prime ($f' = f - \bar{f}$). Quantities normalised by viscous characteristic scales are denoted by a superscript '+' and the subscript 'w' refers to quantities at the wall ($y = 0$). Boundary-layer edge values (subscript 'e') are defined at the minimum y position where the inner-scaled mean z vorticity magnitude falls below a small numerical-noise tolerance ϵ, i.e. $y_e = \min(y : |\bar{\omega}_z^+| < \epsilon)$, and represent the local free-stream state. The 99 % hydrodynamic boundary-layer thickness δ_{99} is determined as $\delta_{99} = (y : \breve{u} = 0.99\breve{u}_e)$, where the pseudo-velocity $\breve{u}_e$ results from wall-normal integration of $-\bar{\omega}_z$ (Spalart & Strelets 2000). Values at $y = \delta_{99}$ are denoted by the subscript '99'.

The present study is structured as follows. The DNS set-up is summarised in § 2, results are discussed in § 3 and concluding remarks are made in § 4.

2. Simulation details

For this study, a DNS of a compressible zero-pressure-gradient TBL is computed at an inlet free-stream Mach number of $M_0 = 2$ with adiabatic wall conditions. As shown by Pirozzoli & Bernardini (2011), use of the van Driest compressibility transformation is well proven to compensate for compressibility effects in adiabatic cases, guaranteeing universality of even higher-order velocity moments as skewness and flatness in the inner layer, see e.g. Guarini *et al.* (2000) and Bernardini & Pirozzoli (2011). Therefore, the conclusions drawn here for the compressible regime apply equally to the incompressible regime, with the relevant caveats highlighted. For all following discussions, the compressible data are considered in their equivalent incompressible representation using viscosity or density scaling. The equivalent form of the incompressible momentum thickness Reynolds number Re_θ is defined as $Re_{\theta_i} = Re_{\delta_2} = (\bar{\mu}_e/\bar{\mu}_w)Re_{\theta_c}$ following van Driest (1956). Here, Re_{θ_c} refers to the momentum thickness Reynolds number as defined before when considering variable density and viscosity, i.e. $Re_{\theta_c} = \theta\bar{u}_e\bar{\rho}_e/\bar{\mu}_e$. With this convention, the inflow Reynolds number of the DNS domain is located at $Re_{\theta_i} \approx 153$, sufficiently low such that the buffer layer effectively abuts the wake. A generous post-inlet relaxation region of $300\delta_0$ assures that the turbulent wake is well recovered from the inflow, yielding an area of interest of $1180 \lessapprox Re_{\theta_i} \lessapprox 5660$, thereby covering the target region in the range $4000 \lessapprox Re_{\theta_i} \lessapprox 5000$. Figure 5 illustrates the domain layout, along with snapshots of the instantaneous flow field.

2.1. *Numerical method*

The DNS has been performed with the compressible code 'NS3D', which solves the three-dimensional dimensionless compressible Navier–Stokes equations together with the continuity and energy equations in conservative formulation on a block-structured curvilinear grid. More details of the code and its numerical procedure can be found in Keller & Kloker (2015, 2017) and Wenzel *et al.* (2018). For spatial discretisation, sixth-order subdomain-compact finite differences in all three directions are used (Keller & Kloker 2013). For time stepping, the classical fourth-order Runge–Kutta scheme is employed, coupled with alternating forward- and backward-biased finite differences for the convective first derivatives (Kloker 1997; Babucke 2009). A spatial tenth-order implicit filter is used to attenuate numerical noise associated with discretisation error. At the solid wall, the flow is treated as fully adiabatic at every time instant with $(\partial T/\partial y)_w = 0$, which suppresses any heat exchange between the wall and fluid; the pressure at the wall is calculated by $(\partial p/\partial y)_w = 0$. The zero-gradient wall conditions for both T, p are calculated using an optimised one-sided fifth-order stencil (Kloker 1997). At the outflow, the time derivative, respectively the complete space operator, is extrapolated with $\partial \boldsymbol{Q}/\partial t|_i = \partial \boldsymbol{Q}/\partial t|_{i-1}$ corresponding to a first-order extrapolation, where $\boldsymbol{Q}$ is the dimensionless conservative solution vector and i represents the grid index in x. At the top of the simulation domain, a characteristic outflow condition is applied (Wenzel 2019); a validation of the zero-pressure-gradient condition can be found in Wenzel *et al.* (2019). At the inflow, a digital-filtering approach is used to generate an unsteady turbulent inflow condition, as discussed in Wenzel *et al.* (2018) and Wenzel (2019). The spanwise

$(L_x \times L_y \times L_z)/\delta_0$	$N_x \times N_y \times N_z$	Δx^+	Δy_w^+	Δy_{99}^+	Δz^+	Re_{θ_i}	Re_τ
$2903.2 \times 118.8 \times 99.7$	$20224 \times 768 \times 1632$	5.7–6.9	0.6–0.7	3.6–4.9	3.0–3.6	1171–5664	360–1469

Table 1. The DNS domain and grid properties. L and N indicate the length and number of grid points per direction. Re ranges and viscous resolutions correspond to the area of interest.

direction is treated as periodic. The specific gas constant R, the ratio of specific heats $\gamma = c_p/c_v = 1.4$ and the Prandtl number $Pr = 0.71$ are constant.

2.2. *Domain grid and dimensions*

The rectilinear grid is constructed as an orthogonal projection of three one-dimensional coordinate arrays. The grid is uniform in x in the domain area of interest such that $\Delta x^+ \lessapprox 7$. The grid is stretched in y such that $\Delta y^+_{w_{max}} \lessapprox 0.7$ and $\Delta y^+_{99} \lessapprox 5$. In z, a uniform grid is defined such that $\Delta z^+ \lessapprox 4$. The domain height L_y and width L_z are dimensioned such that $L_y/\delta 99_{max} \gtrapprox 4$ and $L_z/\delta 99_{max} \gtrapprox 3$, where $\delta 99_{max}$ is the maximum 99 % boundary-layer thickness in the area of interest. Table 1 summarises information about the computational domain. The friction Reynolds number is defined $Re_\tau = \delta_{99}^+ = \delta_{99} u_\tau \bar{\rho}_w/\bar{\mu}_w$, where the friction velocity is $u_\tau = \sqrt{\tau_w/\bar{\rho}_w}$ and the mean wall shear stress is evaluated as $\tau_w = \bar{\mu}_w(\partial \bar{u}/\partial y)_w$. The full grid contains over 25 billion points. The grid stretching and sponge-zone definition is based on the numerical set-up used by Wenzel *et al.* (2018, 2021), which 'may be regarded as essentially devoid of spurious inflow effects' according to the analysis of Ceci *et al.* (2022). After an initial transient phase of $\Delta t/(L_x/u_0) \gtrapprox 2$, a measurement phase is started in which statistical averaging and output of unsteady data are performed. The duration of the measurement phase is such that $\Delta t/(\delta_{99}/u_\tau)_{max} \gtrapprox 12$, where $(\delta_{99}/u_\tau)_{max}$ denotes the maximum i.e. downstream-most local eddy-turnover period within the area of interest.

3. Results and discussion

The following section examines the physical changes that occur in a spatially evolving boundary layer as it develops beyond the low-Re range. To this end, the friction coefficient and turbulent wake are examined, as well as the connection between both quantities to the early development of the logarithmic layer.

3.1. *Introductory comment*

In the following section, mainly the three incompressible DNS/Large-Eddy Simulation (LES) of Schlatter *et al.* (2009), Schlatter & Örlü (2010), Sillero *et al.* (2013) and Eitel-Amor *et al.* (2014) are frequently referred to in order to support the conclusions drawn and to link them with existing data. However, since these data either do not cover the 'blind spot' in the range $4000 \lessapprox Re_\theta \lessapprox 5000$, or inlet independence of the outer layer cannot be ensured within this region, an assessment of the respective data is necessary. To this end, figure 1 illustrates the Re_θ range covered by the simulations mentioned above. For all datasets depicted, the inflow lengths are represented as hatched lines or open markers until either $x \gtrapprox 200\delta_0$ or, if later, where the authors report confidence in shape factor, etc. Although it varies depending on the choice of inflow, $200\delta_0$ roughly represents a typical transit length for necessary turbulent wake recovery, compare with e.g. Sillero *et al.* (2013), where $\sim 250\delta_0$ are required to span $1100 < Re_\theta < 4800$. For the present dataset, the inflow length has been extended to $300\delta_0$ to increase confidence of all following discussions.

https://doi.org/10.1017/jfm.2025.10363 Published online by Cambridge University Press

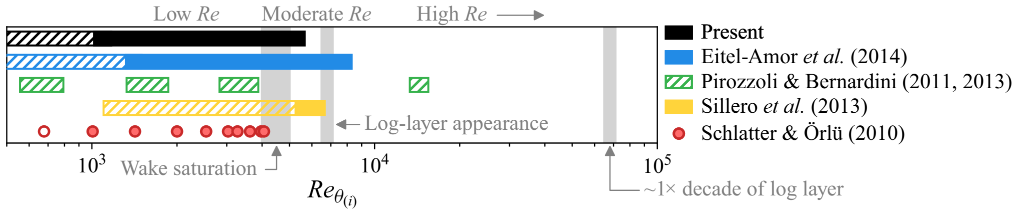

Figure 1. The Re ranges of numerical zero pressure gradient (ZPG) TBL studies. Hatched bars or open markers indicate either $\lessapprox 200\delta_0$ of development space or area upstream of where authors report confidence. The rationale behind the placement (in Re_θ) of the logarithmic-layer 'appearance' and establishment of one decade of wall-normal extent can be found in Appendix A.

Note that such strictness is only necessary for highly sensitive quantities like the turbulent wake or shape factors.

3.2. *Friction coefficient*

In figure 2, the effect of Re on c_f is examined. To compare compressible and incompressible data, both the present compressible DNS as well as the datasets of Pirozzoli & Bernardini (2011, 2013) are transformed into their equivalent incompressible representation (subscript i) by applying the 'van Driest II' transformation, which for an adiabatic wall reduces to

$$c_{f_i} = F_c\, c_{f_c}, \quad F_c = \frac{(\bar{T}_w/\bar{T}_e - 1)}{\arcsin\left(\sqrt{1-\bar{T}_e/\bar{T}_w}\right)^2}. \tag{3.1}$$

Here, c_{f_i} is the transformed incompressible counterpart to c_{f_c}, where $c_{f_c} = 2\tau_w/(\bar{\rho}_e \bar{u}_e^2)$ for compressible cases. In addition to the DNS/LES data already introduced in figure 1, figure 2 shows experimental data from the OFI measurements of Österlund *et al.* (2000) and Nagib *et al.* (2006), representative of the state of the art in direct measurement of τ_w. The low-Re power-law correlation of Smits *et al.* (1983)

$$c_f \approx 0.024\, Re_\theta^{-0.25} \tag{3.2}$$

is plotted, as well as a curve of the form

$$c_f \approx a\, Re_\theta^b + \frac{c}{Re_\theta}, \quad \text{with } a = 0.01844,\ b = -0.2235,\ c = 0.2979. \tag{3.3}$$

The latter simply represents an empirical best fit to the present data to highlight trends in panels (b) and (c). Note that the addition of a c/Re term also better captures the c_f trend for the low-Re region of the dataset of Schlatter & Örlü (2010) rather than a pure power-law relationship. For the high-Re regime, the 'Coles–Fernholz 2' correlation

$$c_f \approx 2\left[\kappa^{-1} \ln(Re_\theta) + C\right]^{-2} \quad \text{with } \kappa = 0.384,\ C = 4.127 \tag{3.4}$$

is plotted (Fernholz & Finley 1996; Nagib *et al.* 2007). Note that $\kappa = 0.384$ is used in accordance with its high-Re calibration in Nagib *et al.* (2007), whereas later $\kappa = 0.41$ is consistently utilised as a fixed constant for cross-comparing primarily low- and moderate-Re datasets.

As was previously shown in a variety of studies, e.g. Schlatter & Örlü (2010), the low-Re numerical data align generally well with the low-Re power-law behaviour in panels (a) and (b), if inlet development regions with more rapidly decreasing c_f are ignored. For $Re_\theta \gtrapprox 5000$, both existing numerical and experimental data clearly confirm

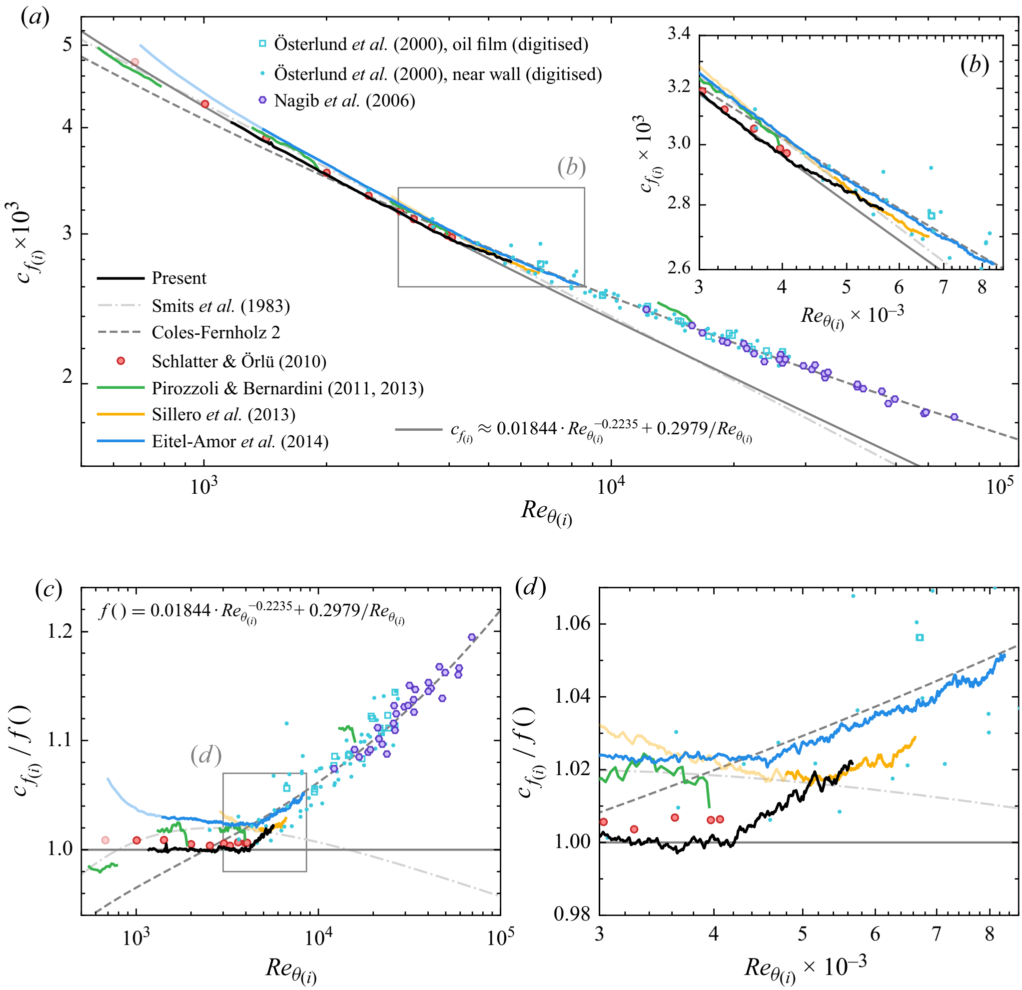

Figure 2. Friction coefficient c_f vs Re_θ with compressible scaling (*a*,*b*) and compensated representation (*c*,*d*). Panels (*b*,*d*) are zooms of (*a*,*c*), respectively.

the high-Re correlation. As indicated by the present newly computed data, represented by the solid black line, the changeover from the low- to the high-Re regime occurs rather abruptly, at least in logarithmic representation. A 'bend' is distinctly visible in the c_f distribution, especially in the zoomed-in representation of panel (*b*). To more closely investigate the abrupt bend in c_f, panels (*c*,*d*) normalise all data of (*a*) by the fitted low-Re correlation. The DNS data of Schlatter & Örlü (2010) terminate precisely at Re_θ where the bend occurs, however, agreement with the newly generated data up to that point supports the plausibility of a sharp bend. Sillero *et al.* (2013) report confidence in their data for $Re_\theta \gtrsim 4800$, precisely the region where their data overlap with the present data. Perhaps the most important evidence for the sharpness of the low-to-moderate Re cross-over comes from LES data of Eitel-Amor *et al.* (2014), which are reported to be independent of initial conditions by $Re_\theta \approx 1500$, but are subject to the uncertainty of a slightly under-resolving numerical grid. Analogous to the present simulation, these data show a notably sharp bend at a comparable Re_θ, although showing a consistent $\sim$2 % offset with respect to the fully resolved incompressible DNS of Schlatter & Örlü (2010).

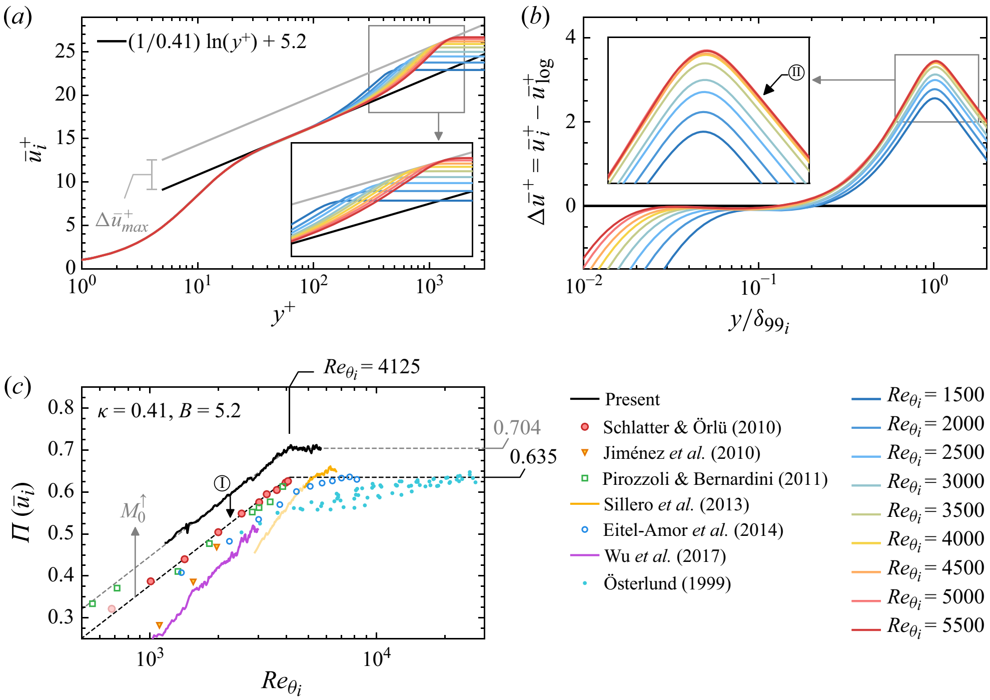

Figure 3. Mean-velocity profiles and wake parameter. The black dotted line in panel (*c*) indicates the fit given in (3.8).

3.3. *Outer layer*

As been shown in a variety of different studies, e.g. Fernholz & Finley (1980) and Nagib & Chauhan (2008); Smits (2024), the turbulent wake appears to develop to a visually Re-independent state at a possible value of approximately $4000 \lessapprox Re_\theta \lessapprox 5000$, which coincides remarkably well with the Re of the present data at which c_f shows a distinct bend. It is explicitly noted, however, that these trends are subject to significant scatter, see e.g. Smits (2024), thus, existing boundary-layer data at large Re indicate this supposed Re-independence is not firmly established. The present section evaluates the wake development as well as its relation to the Reynolds-number range where c_f has been shown to diverge from typical low-Re correlations. To this end, figure 3(*a*,*b*) shows the streamwise velocity $\bar{u}_i$ profiles at several equally spaced Re_{θ_i} stations in inner and outer scaling, where $\bar{u}_i$ is the incompressible-transformed mean streamwise velocity according to van Driest (1951)

$$\bar{u}_i^+ = \int_0^{\bar{u}^+} \sqrt{\frac{\bar{\rho}}{\bar{\rho}_w}}\mathrm{d}\bar{u}^+. \tag{3.5}$$

The wake strength is defined as the local deviation from an assumed 'standard' logarithmic law

$$\bar{u}^+_{\log} = \frac{1}{\kappa}\ln\left(y^+\right) + B, \tag{3.6}$$

with $\kappa = 0.41$, $B = 5.2$. As indicated in figure 3(*a*,*b*), the wake strength $\Delta\bar{u}^+ = \bar{u}_i^+ - \bar{u}_{\log}^+$ saturates for $Re_\theta \gtrapprox 4100$. The collapse, annotated by Ⓘ, is particularly visible in panel (*b*). We note that use of the van Driest transformation increases the velocity profile in the wake region with respect to incompressible data, therefore the wake strength to increases by a Mach-number-dependent, but Reynolds-number-independent offset (Wenzel *et al.* 2018). Thus, conclusions obtained for the present supersonic case reliably transfer to the incompressible regime although the absolute value of the wake strength is increased; implications will be detailed where appropriate. Furthermore, it is emphasised that the tight collapse of the data in the range $4100 \lessapprox Re_{\theta_i} \lessapprox 5660$ spans a respectable Re range of $\Delta Re_{\theta_i} \gtrapprox 1500$ and thus extends notably into the moderate-Re regime. As depicted in figure 3(*c*), the Re dependence of this saturating trend is often quantified by the wake parameter $\varPi$, which is defined as (Coles 1956)

$$\varPi = \frac{\kappa}{2}\left(\bar{u}_{99}^+ - \frac{1}{\kappa}\ln\left(\delta_{99}^+\right) - B\right), \tag{3.7}$$

hence proportional to the wake strength at $y = \delta_{99}$. For all data considered, the same $\kappa = 0.41$, $B = 5.2$ are utilised, which generally shifts high-Re data points to an artificially high $\varPi$ compared with if κ, B, $\varPi$ were fit simultaneously; the assimilated data from Österlund (1999) are most significantly affected by this simplification. It is further noted that some of the scatter observed regarding the wake may likely be associated with the fact that all of the constants in the profile equation are slowly settling into asymptotic values. Furthermore, as addressed in the c_f discussion, the definition of Re_{θ_i} renders the occurrence of the c_f bend notably independent of the Mach number. Thus, differences in panel (*c*) between transformed and incompressible data are only on the ordinate, where transformed compressible data maintain a higher value of $\varPi$ as a consequence of the van Driest transformation. For the present transformed data, $\varPi$ increases $\propto \ln(Re_{\theta_i})$ for $Re_{\theta_i} \lessapprox 4100$ after which it abruptly saturates and stays approximately constant. Note, however, that some caution is warranted about the generalisation of this collapse at higher Re, seeing that most boundary-layer properties evolve logarithmically over decades of Re. Naturally, this change in slope occurs at the same Re_{θ_i} as the c_f bend, which supports the notion that wake convergence – or more specifically the completion of the relative lift of the wake out of the inner layer – is likely the driver for the change in the c_f slope. However, the observed abruptly saturating progression of $\varPi$ seems unfamiliar, as all empirical trend lines known by the authors to date have been formulated by assimilating scattered data to an assumed smooth function (Coles 1962, 1987; Cebeci & Smith 1974; Chauhan *et al.* 2009). Interestingly, partial evidence supporting abrupt wake-convergence behaviour can be gathered from existing data. The dataset of Schlatter & Örlü (2010), for instance, which ends slightly before the expected Re of the bend feature, follows a semi-logarithmic trend up to $Re_\theta \lessapprox 4100$, without displaying any tendency towards smoothly rounding. Data from Sillero *et al.* (2013) are estimated to have an inlet-independent wake – thus high confidence in $\varPi$ – only for $Re_\theta \gtrapprox 4800$, beyond which approximate wake saturation is seen. Thus, if the systematic shift in $\varPi$ for the present transformed data is manually compensated for (grey offset curve in panel (*c*) indicated by Ⓘ), it can be interpreted as a plausible bridge between both datasets, approximated by

$$\varPi(Re_\theta) \approx \begin{cases} -0.8769 + 0.1816\ \ln(Re_\theta) & \text{for } Re_\theta \lessapprox 4125 \\ -0.8769 + 0.1816\ \ln(4125) \approx 0.635 & \text{for } Re_\theta \gtrapprox 4125 \end{cases}, \tag{3.8}$$

indicated by the black dotted line in figure 3(*c*). The LES data of Eitel-Amor *et al.* (2014) are slightly lower compared with the trend curve (corresponding to the higher c_f) but converge towards a consistent $\varPi$ value at higher Re where the effective viscous grid resolution successively increases.

3.4. *Remark*

The previous discussion has confirmed the utility of $\varPi$ as an indicator of the outer-layer similarity, which can be visually observed in figure 3(*a*,*b*). However, the somewhat 'artificial' nature of $\varPi$ as pointed out in Chauhan *et al.* (2009), motivates a further remark. One difficulty (among others) relating to the accurate evaluation of $\varPi$ is its dependence on the log-law constant κ and offset B, which cannot be assumed constant in the lower-Re regime, as scale separation is not sufficient to cultivate a true, unambiguous logarithmic region. At low Re, κ, B must be approximated either by assumption or through fitting the mean profile, neither of which is robust, which itself can lead to scatter among the data. Thus, to support the above discussions, a related metric, as discussed in e.g. Nagib *et al.* (2007) and Sanmiguel Vila *et al.* (2017), is depicted in figure 6 of Appendix B, showing the streamwise evolution of the Rotta–Clauser length scale $\varDelta = \int_0^\infty (\bar{u}_e^+ - \bar{u}^+)\mathrm{d}y$ in relation to δ_{99}. According to classical theory, this wake metric is assumed to become approximately constant as a well-developed outer layer becomes self-similar (like $\varPi$), however, with the benefit of being independent of the pre-supposed existence of a logarithmic layer. Evaluation of $\varDelta/\delta_{99}$ in figure 6 shows the same qualitative trend as $\varPi$ in figure 3(*c*), including sudden saturation at a plateau value. Thus, the resemblance between both metrics strongly supports the discussion above. Additionally, the streamwise development of the wake has been evaluated in Appendix C within the framework of the physically consistent profile form suggested in Monkewitz, Chauhan & Nagib (2007). As with $\varDelta/\delta_{99}$, the general observation regarding the onset of outer-layer velocity profile self-similarity is qualitatively consistent.

3.5. *Logarithmic overlap region*

The previous sections have demonstrated the high sensitivity of the mean-velocity profile to largely unavoidable uncertainties at the inlet boundary, which could potentially obscure fine features of the streamwise evolution of e.g. c_f or the wake strength if sufficient relaxation length is not provided. Following these considerations, attention is turned to the region between the buffer layer and the wake region and how it behaves in conjunction with the wake saturation. For convenience, such will be referred to as the logarithmic overlap layer ('log layer'), although clearly no significant region of precise logarithmic proportionality yet exists at this Re. To this end, the velocity-defect profile $\bar{u}_{i,e}^+ - \bar{u}_i^+ \approx f(y/\delta)$ is illustrated in figure 4(*a*,*c*,*e*) for several Re_{θ_i}, where panel (*c*) is simply a normalisation of panel (*a*) by $f() = 3.752 - 0.41^{-1}\ln(y/\delta)$ for magnification purposes; the constant is fitted after constraining $\kappa = 0.41$. For reference, panel (*e*) focuses once again on the wake region to link the discussion of log layer with the aforementioned lifting process of the wake, where it is clear that, for $Re_{\theta_i} \gtrapprox 4000$, the wake defect profile is highly self-similar with respect to δ_{99_i}. The indicator function $\varXi_i = y^+(d\bar{u}_i^+/dy^+)$ is shown in figure 4(*b*,*d*) along with incompressible reference functions from Monkewitz *et al.* (2007); panel (*d*) is a zoom of panel (*b*).

Most prominently, both panels (*a*) and (*c*) illustrate the development of the defect profile log layer (blue shades) followed by a rather abrupt arrival upon a visually identical slope/offset for $Re_{\theta_i} \gtrapprox 4000$ (white and red shades). Such convergence becomes more visually apparent through examination of $\varXi_i$ in panels (*b*,*d*). Here, a solidification of a

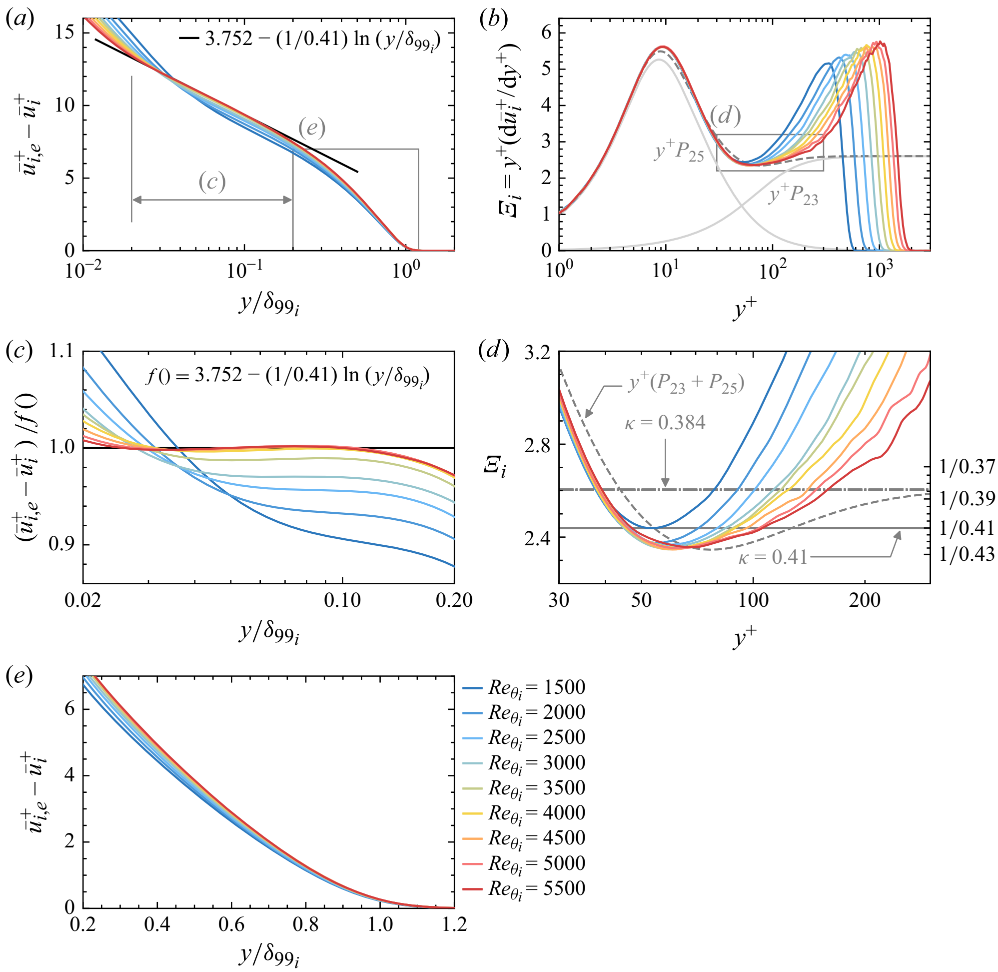

Figure 4. Mean velocity-defect profiles (*a*,*c*,*d*) and diagnostic function (*b*,*d*). For reference, the Padé approximant functions of Monkewitz *et al.* (2007) are plotted with their original parameter values.

local minimum occurs around $y^+ \approx 70$ for the same Re_{θ_i} at which: (i) the bend in c_f occurs, (ii) Π becomes Re-independent and (iii) the velocity-defect log-layer slope and offset become Re-independent. Therefore, present data clearly support that the point of wake convergence at $Re_{\theta_i} \approx 4100$ also marks a state at which a unique characteristic feature in the development of the precursor to the log layer emerges, namely a local minimum in Ξ_i at roughly $y^+ \approx 70$. Note that this conclusion is in line with the LES study by Eitel-Amor *et al.* (2014), where comparable trends have been shown. Further increase in Re would see the Ξ_i curve envelope continually approach a characteristic similar to the $y^+(P_{23} + P_{25})$ curve, eventually flattening out at $\kappa \approx 0.384$ for $y^+ \gtrsim 300$ in the high-Re regime for incompressible flows. It is worth noting, however, that recent studies such as Hoyas *et al.* (2024) and Monkewitz (2024), focusing on channel and pipe flows, have indicated that the indicator function exhibits a slight sensitivity to grid spacing and distribution. This sensitivity, combined with the influence of time averaging, suggests that a more precise discussion of the scaling properties of the overlap layer may not be meaningful at this stage. Nevertheless, the overall trends are largely consistent with the trends suggested by the (incompressible) composite model of Monkewitz *et al.* (2007), with the implications being threefold: first, the transformed compressible and incompressible trends are highly comparable, again adding confidence to previous conclusions. Second, the bend in c_f corresponds to a Reynolds number at which no clear log layer has yet formed, thus it cannot be attributed to the high-Re regime. Third, lack of a log layer in the moderate-Re regime is not attributable to insufficient wake development, although the absence of a Re-independent minimum $\varXi$ might be an indicator.

4. Conclusions

A DNS of a spatially evolving TBL designed to be essentially devoid of spurious inflow effects by the area of interest is discussed, covering the onset of the moderate-Re regime. In the range $4000 \lessapprox Re_\theta \lessapprox 5000$, a surprisingly sharp 'bend' (at least in logarithmic scaling) in c_f is observed, essentially resembling the immediate changeover from established low-Re to high-Re correlations of c_f. Mainly evaluated by comparison with the wake parameter $\varPi$ – as well as additional wake metrics – this 'bend' feature clearly corresponds to the Re position at which the turbulent wake establishes self-similarity with respect to outer characteristic length scales, supporting the understanding that the completed lifting of the wake from the inner layer can be seen as the main driver for the change in the c_f trend. Reasons for this corresponding behaviour are rooted in the outer–inner relationship $\bar{u}_e^+ = \bar{u}_e/u_\tau$ as it evolves with Re, and upon which both c_f and $\varPi$ have a common dependency. As for the c_f distribution, the establishment of self-similarity in the outer layer, which marks the onset of moderate-Re behaviour, occurs surprisingly abruptly, a fact that has likely been obscured by data scatter in previous studies. However, the comparison with DNS/LES data in regions where the independence of the inflow is established at least makes plausible the abruptness of both the c_f curve and the wake convergence. Discussion of the indicator function $\varXi$, namely the establishment of a local minimum in $\varXi$ at roughly $y^+ \approx 70$, implies that the point of wake convergence also marks a unique state in the development of the precursor to the log layer which only becomes significant in thickness at higher Re. Consequently, the abrupt change in state of the TBL, perhaps the most meaningful consequence of which is the rapid change in the $c_f(Re)$ progression, appears to be a characteristic trait of the onset of moderate-Re behaviour. While speculative, possible reasons for this rapid change in Re-behaviour could be associated with large-wavelength fluctuations, probably originating from the outer layer carrying free-stream momentum, which are transported to and interact with the wall with increasing Re. The increasing 'uprightness' of the $\bar{u}^+(y^+)$ wake profile is thus consistent as, on average, such structures more efficiently capture – and/or are more able to 'hold on to' – free-stream momentum. Such likely ties into the well-studied story of increasing scale separation and eventual interaction of large-scale 'superstructures' of the outer layer with the wall. However, although this discussion clearly will be part of the correct answer, it does not yet fully explain the abruptness of the c_f bend.

Funding. This work was supported by the Deutsche Forschungsgemeinschaft (DFG) in the context of grants RI680/49-1 and WE6803/5-3. The provision of computational resources on HPE Apollo 'Hawk' and NEC SX-Aurora TSUBASA by the Federal High Performance Computing Center Stuttgart (HLRS) under grant GCS-Lamt, project 28956, is gratefully acknowledged.

Declaration of interests. The authors report no conflict of interest.

Data availability statement. The data that support the findings of this study are openly available at: https://doi.org/10.18419/darus-4165.

https://doi.org/10.1017/jfm.2025.10363 Published online by Cambridge University Press

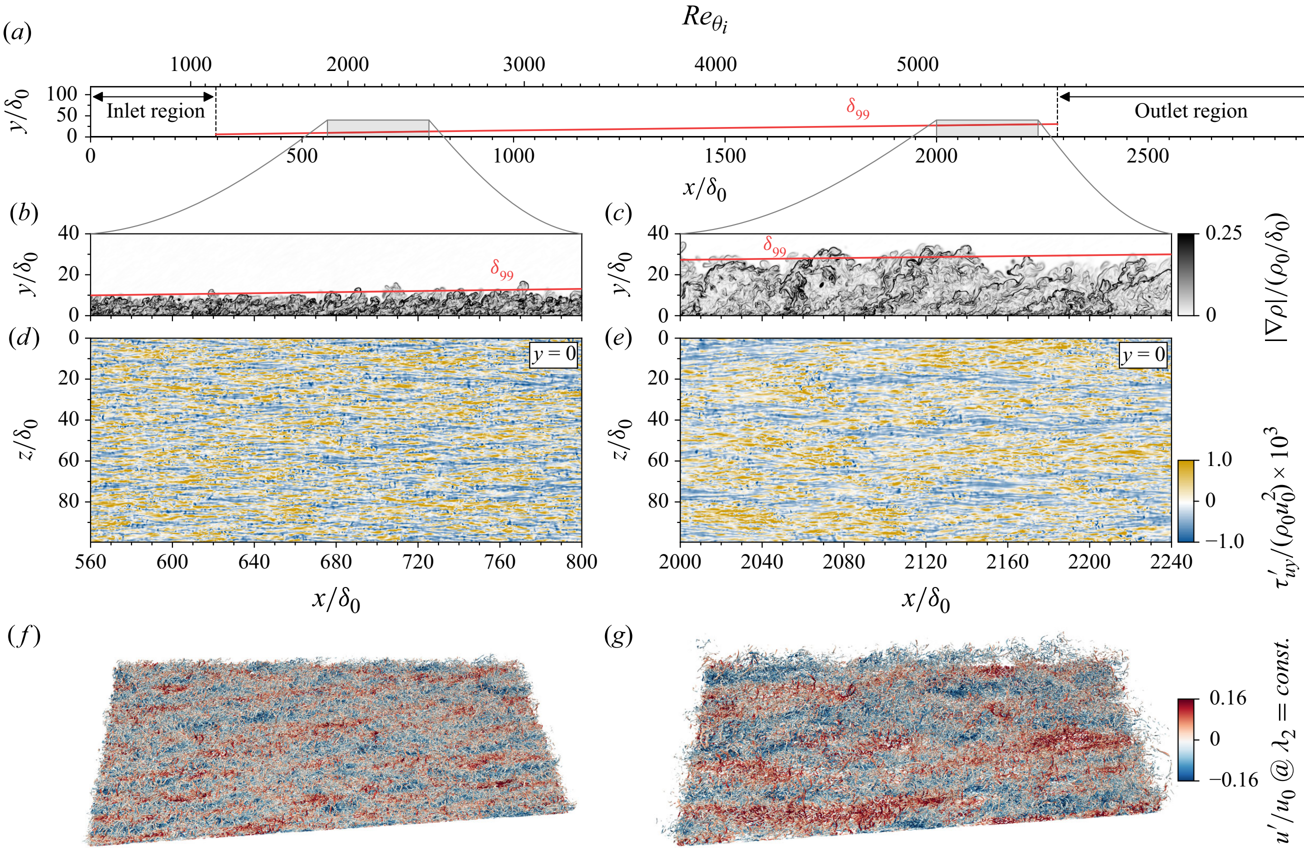

Figure 5. Visualisation of the instantaneous flow. Panel (*a*) is a side view of the full domain geometry. Panels (*b*,*c*) show the magnitude of the density gradient. Panels (*d*,*e*) show mean-removed shear stress τ'_{uy} at the wall. Panels (*f*,*g*) show isosurfaces of λ_2 criterion coloured by mean-removed streamwise velocity u'. All plots are provided at two different Re, namely upstream (left) and downstream (right) of the point of wake saturation.

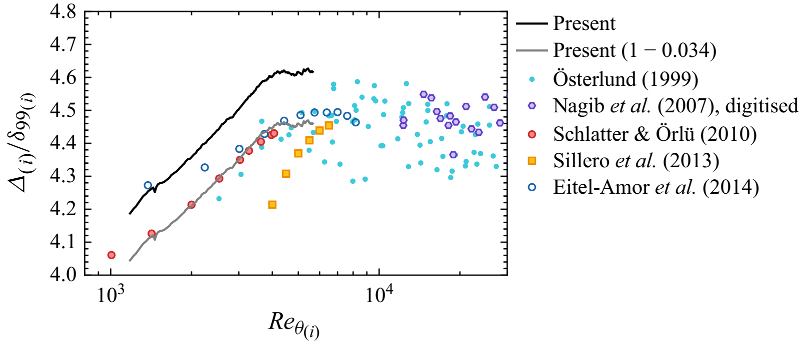

Figure 6. Streamwise evolution of the Rotta-Clauser length scale Δ normalised by δ_{99}.

Appendix A. Estimation of log-layer development

The representation of the viscous-scaled inner profile from Monkewitz *et al.* (2007) shows that the overlap region does not faithfully adhere to a 'true' logarithmic trend (i.e. $\varXi = y^+(\mathrm{d}\bar{u}^+/\mathrm{d}y^+) \approx const.$) until $y^+ \gtrsim 300$. Note that this bound is a matter of tolerances; estimates include $y^+ \gtrsim 100$ (Hutchins & Marusic 2007), $y^+ \gtrsim 200$ (Nagib *et al.* 2007) and $y^+ \gtrsim 600$ (Zagarola & Smits 1998; McKeon *et al.* 2004) for pipe flows, among others. Marusic *et al.* (2013) have determined $y^+ = 3Re_\tau^{0.5}$ as a conservative limit using pipe and boundary-layer data. Assuming that the logarithmic region ends at roughly $y/\delta_{99} \gtrsim 0.15$ (Hutchins & Marusic 2007; Vallikivi, Hultmark & Smits 2015), it follows that this wall-normal position must be greater than or equal to the mentioned start of the log layer. Setting $0.15\delta_{99} \approx 300\delta_\nu$ yields $Re_\tau \approx 2000$ as an effective estimate of the minimum Re at which the log layer could arguably be present with $Re_\tau = \delta_{99}/\delta_\nu = \delta_{99}u_\tau/\bar{\nu}_w$. To convert to Re_θ for the incompressible ZPG case a correlation $Re_\tau(Re_\theta)$ is required. Regression of data from Schlatter & Örlü (2010) yields $Re_\tau \approx 0.6966Re_\theta^{0.9036}$, whereas their own reported estimation (based on other DNS and experiments) is $Re_\tau \approx 1.13Re_\theta^{0.843}$. Regression of high-$Re$ data has led Smits (2024) to conclude $Re_\theta \approx 3.241Re_\tau$. Figure 1 therefore utilises $Re_\theta \approx 6800 \pm 300$ as a rough estimate for the 'appearance' of a log layer. A further milestone of TBL development is the establishment of a log layer spanning one decade of wall-normal distance, which can be estimated as $10\times$ the Re_τ of log-layer appearance, presently $Re_\tau \approx 20\,000$. Assuming $Re_\theta \propto Re_\tau^{1.0}$ (Smits 2024), this yields $Re_\theta \approx 68\,000 \pm 3000$. Both estimates are plotted as grey bars in figure 1. It should be noted that the present estimation is unique to boundary layers; mean-velocity profiles of internal canonical flows have different Re-scaling behaviour (Monkewitz & Nagib 2023).

Appendix B. Alternative wake metric

Figure 6 evaluates the streamwise evolution of the Rotta–Clauser length scale $\Delta = \int_0^\infty (\bar{u}_e^+ - \bar{u}^+)\mathrm{d}y$ normalised by δ_{99}, where $\bar{u}_i$ (Eq. 3.5) is used for compressible data. Note that, as for $\varPi$ in § 3.3, transformed compressible data are higher compared with incompressible reference data as a consequence of the van Driest transformation, as reflected by the black solid line. Following work by Nagib *et al.* (2007), the ratio Δ/δ_{99} can be seen as a well-suited metric to assess the evolution of the TBL's outer region towards a self-similar state. If the van Driest transformed data are manually shifted downward to allow visual comparison with purely incompressible data with the same reasoning as for $\varPi$ before (grey dashed line), the results in figure 6 closely resemble the trends already discussed for $\varPi$ in figure 3(*c*), namely that Δ/δ_{99} increases $\propto \ln(Re_{\theta_i})$ for $Re_{\theta_i} \lesssim 4100$,

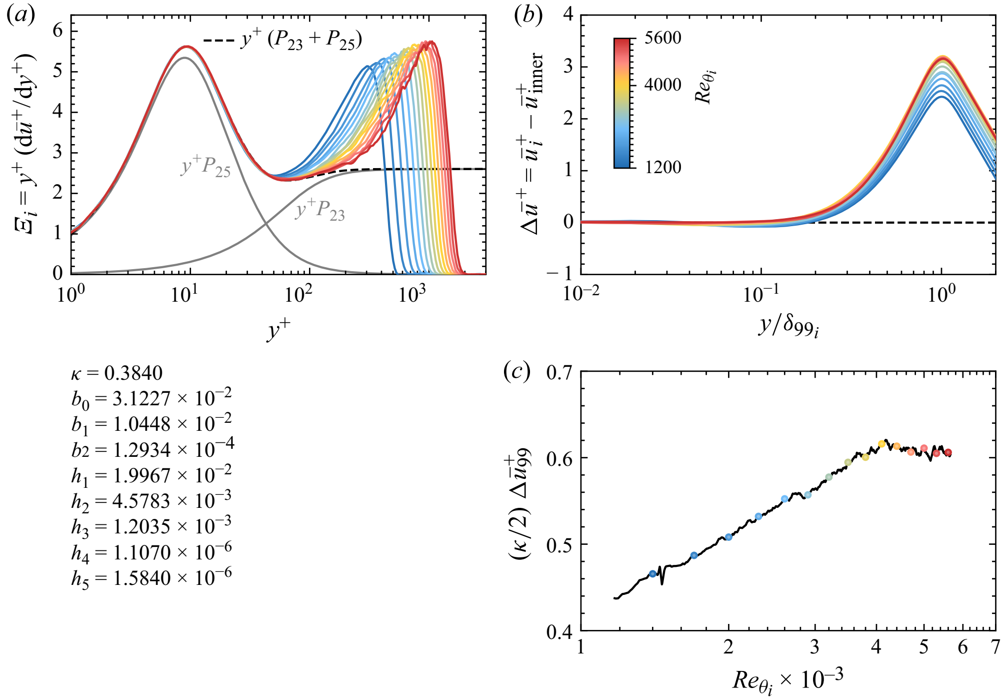

Figure 7. Indicator function (*a*) and fitted polynomial-based 'inner' function of Monkewitz *et al.* (2007). The resulting parameters of the fitted function are provided. Panel (*b*) shows the mean streamwise velocity profile with fitted inner profile subtracted. The development of the resulting wake parameter analogue vs *Re* is shown in panel (*c*).

after which it plateaus at $4.4 \lessapprox \Delta/\delta_{99} \lessapprox 4.5$. Further discussion can be found in Nagib *et al.* (2007) and Sanmiguel Vila *et al.* (2017). As well as for Π, partial evidence supporting the abrupt onset of wake self-similarity can be gathered from existing data, especially the dataset by Schlatter & Örlü (2010).

Appendix C. Outer layer evaluated with respect to polynomial inner-layer fit

Figure 3 (*b*,*c*) has computed $\Delta\bar{u}^+$ and Π based on the classical composite formulation of Coles (1956) with fixed κ, B mainly for clarity of comparison, given that 1) the overlap layer in low-*Re* profiles has no appreciable region of constant Ξ and 2) the progression of Π (3.7) vs *Re* is of primary relevance to the conclusions of the present work, not necessarily the absolute value. Monkewitz *et al.* (2007) have developed an elegant composite profile formulation having consistent physical properties based on rigorous scaling arguments. For the present evaluation of the viscous-scaled outer-layer profile, we use the inner-layer profile formulation of Monkewitz *et al.* (2007), consisting of two summed Padé polynomial approximants (Monkewitz & Nagib 2006). Figure 7(*a*) corresponds to figure 4(*b*); the highest-*Re* profile plotted has been used to fit a curve $y^+(P_{23}+P_{25})$ as a reference indicator function Ξ. The outer region of the (differenced) mean-velocity profile is illustrated in figure 7(*b*), analogous to figure 3(*b*), with $\Delta\bar{u}^+$ presently computed as the difference of $\bar{u}_i^+$ with respect to $\bar{u}_{\mathrm{inner}}^+$, the wall-normal integral of $(P_{23}+P_{25})$, rather than $\bar{u}_{\mathrm{log}}^+$. Figure 7(*c*) plots the resulting $(\kappa/2)\,\Delta\bar{u}_{99}^+$ vs Re_{θ_i}. Figures 7(*b*,*c*) both confirm the effective collapse of the outer-layer profile onto a common form in outer scaling for $Re \gtrapprox 4100$, in line with the general conclusions of the present work and Appendix B.

References

Babucke, A. 2009 Direct numerical simulation of noise-generation mechanisms in the mixing layer of a jet. PhD thesis, University of Stuttgart, Germany.

Bernardini, M. & Pirozzoli, S. 2011 Wall pressure fluctuations beneath supersonic turbulent boundary layers. *Phys. Fluids* **23** (8), 085102.

Cebeci, T. & Smith, A.M.O. 1974 Analysis of turbulent boundary layers. In *Applied Mathematics and Mechanics*, vol. 15, Academic Press.

Ceci, A., Palumbo, A., Larsson, J. & Pirozzoli, S. 2022 Numerical tripping of high-speed turbulent boundary layers. *Theor. Comp. Fluid Dyn.* **36** (6), 865–886.

Chauhan, K.A., Monkewitz, P.A. & Nagib, H.M. 2009 Criteria for assessing experiments in zero pressure gradient boundary layers. *Fluid Dyn. Res.* **41** (2), 021404.

Coles, D. 1956 The law of the wake in the turbulent boundary layer. *J. Fluid Mech.* **1** (2), 191–226.

Coles, D. 1987 Coherent structures in turbulent boundary layers. In *Perspectives in Turbulence Studies*, (ed. Hans Ulrich M. & Bradshaw P.), pp. 93–114. Springer.

Coles, D.E. 1962 The turbulent boundary layer in a compressible fluid, Tech. Rep. R-403-PR. RAND Corporation.

van Driest, E.R. 1951 Turbulent boundary layer in compressible fluids. *J. Aeronaut. Sci.* **18** (3), 145–160.

van Driest, E.R. 1956 The problem of aerodynamic heating. *Aeronaut. Engng Rev.* **15** (10), 26–41.

Eitel-Amor, G., Örlü, R. & Schlatter, P. 2014 Simulation and validation of a spatially evolving turbulent boundary layer up to $Re_\theta = 8300$. *Intl J. Heat Fluid Flow* **47**, 57–69.

Erm, L.P. & Joubert, P.N. 1991 Low-Reynolds-number turbulent boundary layers. *J. Fluid Mech.* **230**, 1–44.

Fernholz, H.H. & Finley, P.J. 1980 A critical commentary on mean flow data for two-dimensional compressible turbulent boundary layers, Tech. Rep. 253. Advisory Group for Aerospace Research & Development.

Fernholz, H.H. & Finley, P.J. 1996 The incompressible zero-pressure-gradient turbulent boundary layer: an assessment of the data. *Prog. Aerosp. Sci.* **32** (4), 245–311.

Fernholz, H.H., Janke, G., Schober, M., Wagner, P.M. & Warnack, D. 1996 New developments and applications of skin-friction measuring techniques. *Meas. Sci. Technol.* **7** (10), 1396–1409.

Guarini, S.E., Moser, R.D., Shariff, K. & Wray, A. 2000 Direct numerical simulation of a supersonic turbulent boundary layer at mach 2.5. *J. Fluid Mech.* **414**, 1–33.

Hoyas, S., Vinuesa, R., Schmid, P. & Nagib, H. 2024 Sensitivity study of resolution and convergence requirements for the extended overlap region in wall-bounded turbulence. *Phys. Rev. Fluids* **9** (8), L082601.

Hutchins, N. & Marusic, I. 2007 Large-scale influences in near-wall turbulence. *Phil. Trans. R. Soc. A: Math. Phys. Engng Sci.* **365** (1852), 647–664.

Jiménez, J., Hoyas, S., Simens, M.P. & Mizuno, Y. 2010 Turbulent boundary layers and channels at moderate reynolds numbers. *J. Fluid Mech.* **657**, 335–360.

Keller, M.A. & Kloker, M.J. 2013 Direct numerical simulations of film cooling in a supersonic boundary-layer flow on massively-parallel supercomputers. In *Sustained Simulation Performance 2013*, (ed. Resch M.M., Bez W., Focht E., Kobayashi H. & Kovalenko Y.), pp. 107–128. Springer International Publishing.

Keller, M.A. & Kloker, M.J. 2015 Effusion cooling and flow tripping in laminar supersonic boundary-layer flow. *AIAA J.* **53** (4), 902–919.

Keller, M.A. & Kloker, M.J. 2017 Direct numerical simulation of foreign-gas film cooling in supersonic boundary-layer flow. *AIAA J.* **55** (1), 99–111.

Kloker, M.J. 1997 A robust high-resolution split-type compact FD scheme for spatial direct numerical simulation of boundary-layer transition. *Flow Turbul. Combust.* **59**, 353–377.

Marusic, I., Monty, J.P., Hultmark, M. & Smits, A.J. 2013 On the logarithmic region in wall turbulence. *J. Fluid Mech.* **716**, R3.

McKeon, B.J., Li, J., Jiang, W., Morrison, J.F. & Smits, A.J. 2004 Further observations on the mean velocity distribution in fully developed pipe flow. *J. Fluid Mech.* **501**, 135–147.

Monkewitz, P.A. 2024 On the difficulty of determining Kármán 'constants' from direct numerical simulations. *Phys. Fluids* **36** (4), 045162.

Monkewitz, P.A., Chauhan, K.A. & Nagib, H.M. 2007 Self-consistent high-Reynolds-number asymptotics for zero-pressure-gradient turbulent boundary layers. *Phys. Fluids* **19** (11), 115101.

Monkewitz, P.A. & Nagib, H.M. 2006 The asymptotic structure of high-Reynolds number boundary layers. In *IUTAM Symposium on One Hundred Years of Boundary Layer Research*, (ed. Meier G.E.A., Sreenivasan K.R. & Heinemann H.-J.), pp. 355–362. Springer Netherlands.

MONKEWITZ, P.A. & NAGIB, H.M. 2023 The hunt for the Kármán 'constant' revisited. *J. Fluid Mech.* **967**, A15.

NAGIB, H.M. & CHAUHAN, K.A. 2008 Variations of von Kármán coefficient in canonical flows. *Phys. Fluids* **20** (10), 101518.

NAGIB, H.M., CHAUHAN, K.A. & MONKEWITZ, P.A. 2007 Approach to an asymptotic state for zero pressure gradient turbulent boundary layers. *Phil. Trans. R. Soc. A: Math. Phys. Engng Sci.* **365** (1852), 755–770.

NAGIB, H.M., CHRISTOPHOROU, C. & MONKEWITZ, P.A. 2006 High Reynolds Number Turbulent Boundary Layers Subjected to Various Pressure-Gradient Conditions. In IUTAM Symposium on One Hundred Years of Boundary Layer Research, (ed. Meier G.E.A., Sreenivasan K.R. & Heinemann H.-J.), pp. 383–394. Springer Netherlands.

ÖSTERLUND, J.M. 1999 Experimental studies of zero pressure-gradient turbulent boundary layer flow. PhD thesis, Royal Institute of Technology, Department of Mechanics, Sweden.

ÖSTERLUND, J.M., JOHANSSON, A.V., NAGIB, H.M. & HITES, M.H. 2000 A note on the overlap region in turbulent boundary layers. *Phys. Fluids* **12** (1), 1–4.

PANTON, R.L. 2005 Review of wall turbulence as described by composite expansions. *Appl. Mech. Rev.* **58** (1), 1–36.

PIROZZOLI, S. & BERNARDINI, M. 2011 Turbulence in supersonic boundary layers at moderate Reynolds number. *J. Fluid Mech.* **688**, 120–168.

PIROZZOLI, S. & BERNARDINI, M. 2013 Probing high-Reynolds-number effects in numerical boundary layers. *Phys. Fluids* **25** (2), 021704.

SANMIGUEL VILA, C., VINUESA, R., DISCETTI, S., IANIRO, A., SCHLATTER, P. & ÖRLÜ, R. 2017 On the identification of well-behaved turbulent boundary layers. *J. Fluid Mech.* **822**, 109–138.

SCHLATTER, P. & ÖRLÜ, R. 2010 Assessment of direct numerical simulation data of turbulent boundary layers. *J. Fluid Mech.* **659**, 116–126.

SCHLATTER, P. & ÖRLÜ, R. 2012 Turbulent boundary layers at moderate Reynolds numbers: inflow length and tripping effects. *J. Fluid Mech.* **710**, 5–34.

SCHLATTER, P., ÖRLÜ, R., LI, Q., BRETHOUWER, G., FRANSSON, J.H.M., JOHANSSON, A.V., ALFREDSSON, P.H. & HENNINGSON, D.S. 2009 Turbulent boundary layers up to $Re_\theta = 2500$ studied through simulation and experiment. *Phys. Fluids* **21** (5), 051702.

SILLERO, J.A., JIMÉNEZ, J. & MOSER, R.D. 2013 One-point statistics for turbulent wall-bounded flows at Reynolds numbers up to $\delta^+ \approx 2000$. *Phys. Fluids* **25** (10), 105102.

SMITS, A.J. 2024 Wall-wake laws for the mean velocity and the turbulence. *J. Fluid Mech.* **989**, A15.

SMITS, A.J., MATHESON, N. & JOUBERT, P.N. 1983 Low-Reynolds-number turbulent boundary layers in zero and favorable pressure gradients. *J. Ship Res.* **27** (03), 147–157.

SPALART, P.R. & STRELETS, M.K.H. 2000 Mechanisms of transition and heat transfer in a separation bubble. *J. Fluid Mech.* **403**, 329–349.

VALLIKIVI, M., HULTMARK, M. & SMITS, A.J. 2015 Turbulent boundary layer statistics at very high Reynolds number. *J. Fluid Mech.* **779**, 371–389.

WENZEL, C. 2019 DNS of compressible turbulent boundary layers: pressure-gradient influence and self-similarity. PhD thesis, University of Stuttgart, Germany.

WENZEL, C., GIBIS, T., KLOKER, M. & RIST, U. 2019 Self-similar compressible turbulent boundary layers with pressure gradients. Part 1. Direct numerical simulation and assessment of Morkovin's hypothesis. *J. Fluid Mech.* **880**, 239–283.

WENZEL, C., SELENT, B., KLOKER, M. & RIST, U. 2018 DNS of compressible turbulent boundary layers and assessment of data/scaling-law quality. *J. Fluid Mech.* **842**, 428–468.

WENZEL, C., VOGLER, P., PETER, J.M.F., KLOKER, M.J. & RIST, U. 2021 Application of a JPEG 2000-based data compression algorithm to DNS of compressible turbulent boundary layers Up to $\mathrm{Re}_\theta = 6600$. In *High Performance Computing in Science and Engineering '20*, (ed. Nagel, W.E., Kröner, D.H. & Resch, M.M.), pp. 295–313. Springer International Publishing.

WU, X., MOIN, P., WALLACE, J.M., SKARDA, J., LOZANO-DURÁN, A. & HICKEY, J.-P. 2017 Transitional–turbulent spots and turbulent–turbulent spots in boundary layers. *Proc. Natl Acad. Sci. USA* **114** (27), E5292–E5299.

ZAGAROLA, M.V. & SMITS, A.J. 1998 Mean-flow scaling of turbulent pipe flow. *J. Fluid Mech.* **373**, 33–79.